Original Article

JCBFM

Journal of Cerebral Blood Flow & Metabolism
2022, Vol. 42(4) 656–666

DOI: 10.1177/0271678X211058285
journals.sagepub.com/home/jcbfm

Quantification of monoacylglycerol lipase and its occupancy by an exogenous ligand in rhesus monkey brains using [^{18}F]T-401 and PET

Yasushi Hattori[1], Chie Seki[2], Jun Maeda[2], Yuji Nagai[2], Kazunobu Aoyama[1], Ming-Rong Zhang[2], Takafumi Minamimoto[2], Tatsuki Koike[1] and Makoto Higuchi[2]

Abstract

Monoacylglycerol lipase (MAGL) is a cytosolic serine hydrolase that cleaves monoacylglycerols into fatty acids and is a potential target for the novel treatment of CNS disorders related to the endocannabinoid system and neuroinflammation. We have developed [^{18}F]T-401 as a selective Positron emission tomography (PET) imaging agent for MAGL. In this study, we determined an analytical method to quantify MAGL availability and its occupancy by an exogenous inhibitor in rhesus monkey brains using [^{18}F]T-401-PET. In rhesus monkeys, regional time-activity curves were described well when using an extended 2-tissue compartment model that accommodated the formation of a radiometabolite in the brain. This model yielded reliable estimates of the total distribution volume (V_T), and the rank order of V_T was consistent with known regional activity of MAGL enzyme in primates. The pretreatment of monkeys with JW642 resulted in a dose-dependent reduction of [^{18}F]T-401 retentions in the brain, and V_T. Lassen's graphical analysis indicated a V_{ND} of 0.69 mL/cm^3 and a plasma JW642 concentration of 126 ng/mL for inhibiting the specific binding by 50%. [^{18}F]T-401 and the method established can be used for quantification of MAGL in healthy brain and in disease conditions, and is suitable for evaluations of target engagement at cerebral MAGL.

Keywords

Monoacylglycerol lipase (MAGL), positron emission tomography (PET), [^{18}F]T-401, non-human primates, occupancy

Received 31 January 2021; Revised 8 October 2021; Accepted 17 October 2021

Introduction

Endocannabinoid neurotransmission in the central and peripheral nervous systems is a lipid signaling network, which consists of CB1 and CB2 cannabinoid receptors and their endogenous fatty acid ligands.[1] Dysfunctions of this system have been reported to be involved in a broad spectrum of organic and systemic disorders, including obesity, immunological dysfunction, metabolic syndromes, psychiatric conditions, and neurodegenerative diseases.[2–4] The primary endogenous ligands for CB1 and CB2 receptors are N-arachidonoyl ethanolamine (AEA) and 2-arachidonoylglycerol (2-AG). Unlike vesicular neurotransmissions, AEA and 2-AG are biosynthesized by the hydroxylation of membrane phospholipids on demand in response to neuronal activity and are rapidly deactivated through hydrolysis catalyzed by fatty acid amide hydrolase (FAAH) and monoacylglycerol lipase (MAGL), respectively.[1]

[1]Takeda Pharmaceutical Company Limited, Kanagawa, Japan
[2]National Institutes for Quantum Science and Technology, Chiba, Japan

Corresponding authors:
Chie Seki, National Institutes for Quantum Science and Technology, Institute for Quantum Medical Science, 4-9-1, Anagawa, Inage-ku, Chiba-shi, Chiba 263-8555, Japan.
Email: seki.chie@qst.co.jp

Tatsuki Koike, Takeda Pharmaceutical Company Limited, 26-1 Muraoka-Higashi, 2-Chome, Fujisawa, Kanagawa 251-8555, Japan.
Email: tatsuki.koike@takeda.com

MAGL is a cytosolic serine hydrolase that cleaves monoacylglycerols into fatty acids and glycerol and is responsible for ≈85% of the 2-AG hydrolysis.[5,6] Thus, the pharmacological inhibition of MAGL increases 2-AG levels, which leads to the activation of the endocannabinoid neurotransmission and consequent antinociceptive, anxiolytic, and anti-emetic responses.[7] MAGL inhibition also decreases arachidonic acid (AA) levels, which is a pain- and inflammation-inducing prostaglandin precursor, which results in anti-inflammatory and neuroprotective effects in the brain.[8,9] Thus, MAGL is a promising target for the treatment of neuropsychiatric disorders in which the endocannabinoid system and neuroinflammation are mechanistically implicated.[10,11] Indeed, a Phase 2 study has been initiated to evaluate efficacies of an orally active human MAGL inhibitor, ABX-1431, for the treatment of patients with Tourette syndrome, which is a neurodevelopmental disorder characterized by sudden, involuntary movements and vocal tics.[12]

Positron emission tomography (PET) is a non-invasive molecular imaging modality that allows to quantify physiological and pathological processes in living subjects. PET imaging using a specific radioprobe for MAGL could potentially help assess the abundance of MAGL and its alterations in homeostatic and diseased conditions. In addition, this modality can be utilized to determine the occupancy of MAGL by a therapeutic MAGL inhibitor that competes with the PET probe for a binding pocket, providing critical information for the target engagement of this candidate drug.

We have recently reported the discovery, radiosynthesis, and *in vitro* and *in vivo* evaluations of [^{18}F]T-401 as the first PET imaging agent that reversibly and selectively binds to MAGL in living rodent and non-human primate brains.[13] In this study, we aimed to establish an analytical method to quantify [^{18}F]T-401 binding in the rhesus monkey brain. Then, the assaying procedure was applied to the PET measurements of MAGL occupancy by a selective inhibitor, JW642.[14]

Materials and methods

Chemicals

[^{18}F]T-401 was synthesized by the [^{18}F]fluorination of a nitro precursor with [^{18}F]KF/Kryptofix 222 (Merck), as previously described.[13] Non-radioactive T-401 and compound 4f were synthesized by Takeda Pharmaceutical Company Limited, as previously described.[13,15] JW642 was purchased from Tocris Bioscience (Bristol, UK) (Supplemental Figure 1).

Animal experiments

All procedures involving animals and their care were approved by the Animal Ethics Committee of the National Institutes for Quantum Science and Technology. All the animal study data were reported according to ARRIVE guidelines (Animal Research: Reporting in Vivo Experiment).

Male C57BL/6JJcl mice and MAGL-KO mice used were generated by Takeda Pharmaceutical Company Limited.[13] All animal experiments were performed according to the recommendations of the Committee for the Care and Use of Laboratory Animals, former National Institute of Radiological Sciences. Animals were maintained and handled in accordance with the recommendations of the National Institute of Health and the guidelines of the former National Institute of Radiological Sciences. Three male rhesus monkeys (*Macaca mulatta*, M185: age 10 y.o.; M187, age 10-11 y.o.; M197 age 8 y.o.; 5–7 kg) were used for PET studies.

Baseline and blocking PET studies in rhesus monkeys

Rhesus monkeys were initially anesthetized with an intramuscular injection of ketamine (10 mg/kg) and then intubated and kept anesthetized with 1–2% isoflurane. An electrocardiogram and blood oxygen saturation levels of the animals were monitored using Life Scope VS (Nihonkohden, Tokyo), and the body temperature was maintained using a heating pad throughout the experiment. PET scans were performed using a micro PET Focus 220 small-animal scanner (Siemens Medical Solutions USA, Malvern, USA). Following transmission scans for attenuation correction using a ^{68}Ge–^{68}Ga point source, emission scans were performed for 120 min in a 3D list-mode immediately after the i. v. injection of [^{18}F]T-401 (356 ± 50 MBq, 343 ± 68 GBq/μmol), as previously described.[13] All list-mode data were sorted into 3D sinograms, which were then Fourier-rebinned into 2D sinograms (frames: 12×10 s, 6×30 s, 5×1 min, 5×2 min, and 20×5 min). Then, images were reconstructed with filtered back-projection using a Hanning filter with a cut-off at the Nyquist frequency (0.5 mm^{-1}). To quantify the occupancy of MAGL by JW642 in the brain, JW642 was intravenously injected into a monkey (M187) at doses of 0.01, 0.03, 0.1, and 0.3 mg/kg 5 min before the injection of [^{18}F]T-401.

To determine an arterial input function, serial 24 blood samples (1–2.5 mL) were collected from the saphenous artery throughout the emission scan after the i. v. injection of [^{18}F]T-401. An aliquot of plasma was separated with a refrigerated centrifuge ($15000 \times g$, 3 min, 4 °C). The plasma and whole blood radioactivity

concentrations of the blood samples were measured with an auto-gamma counter (WIZARD 1480, Perkin Elmer). In addition to the measurement of radioactivity concentration, the plasma samples collected at 2, 5, 10, 30, 60, 90, and 120 min were used to quantify a fraction of unchanged [^{18}F]T-401. All samples were centrifuged and treated, as previously reported.[16] An aliquot of the supernatant (100–300 µL) prepared from the plasma was analyzed according to the following HPLC condition: column, Atlantis T3 3 µm 4.6 × 150 mm; mobile phase, acetonitrile/H_2O (40/60); flow rate, 1.0 mL/min; and detection wavelength, 254 nm (Supplemental Figure 2). The ratio of unchanged [^{18}F]T-401 to total radioactivity (corrected for decay) was calculated according to peak areas on the HPLC chromatogram. Then, the metabolite-corrected arterial plasma input function was determined with plasma radioactivity concentrations and unmetabolized fractions.

In the JW642 blocking study, plasma samples obtained at 5 s and 30, 60, 90, and 120 min after the [^{18}F]T-401 injection were analyzed by liquid chromatography coupled to tandem mass spectrometry (LC-MS/MS).

Quantification of [^{18}F]T-401 binding and its blockade by the JW642 pretreatment in monkey brains

PET images were coregistered to individual T1-weighted brain images, and regions of interest (ROIs) were placed on the frontal cortex, striatum, cerebellum, occipital cortex, hippocampus, thalamus, and pons, and regional time-activity curves (TACs) were obtained. Because there was no region entirely devoid of MAGL in the brain, the total volume of distribution (V_T) was calculated with an arterial input function to evaluate the [^{18}F]T-401 binding. The data sets at baseline and under blockade by the maximum dose of JW642 (0.3 mg/kg) were used to determine an optimal kinetic model to quantify V_T. Several compartment models were tested, and a model that best describes observed TACs was chosen based on the Akaike's information criterion (AIC),[17] model selection criterion (MSC),[18] and goodness of fit with F-statistics.[18] The time-stability of V_T was also assessed to evaluate whether the scan duration was adequate to calculate V_T. V_T values were estimated by truncating dynamic data from 120 min to 60 min. The kinetic analysis was performed with the PMOD software Ver. 3.7. MAGL occupancy (Occ) by JW642 was quantified using Lassen's plot as follows:

$$V_T^{\text{baseline}} - V_T^{\text{JW642}} = \text{Occ}\ \left(V_T^{\text{baseline}} - V_{ND}\right)$$

where V_T^{baseline} and V_T^{JW642} are regional V_T values at baseline and after the JW642 treatment, respectively; V_{ND} is non-displaceable distribution volume, and Occ is occupancy. Occ was calculated for each JW642 dose. To investigate relationships between the MAGL Occ by JW642 and concentration of JW642 in plasma, we sampled plasma from a monkey prior to PET scans in the blockade experiment and measured concentrations of JW642 by LC-MS. Then, the concentration of JW642 at the initiation of the PET scan was calculated by extrapolating observed values using the one-phase decay model (Graph Pad Prizm 6, GraphPad Software, Inc.). The relationship between the dose of JW642 and Occ induced by this dose was analyzed to determine ED_{50} (effective dose of JW642 inducting 50% occupancy of MAGL) with a single-site binding model using the GraphPad Prism 6 software (GraphPad Software).

Identification of metabolites of T-401 in mice

To obtain metabolic information on T-401 supplementary to the determination of an optimal kinetic model in monkeys, we assayed unmetabolized and metabolized T-401 in mouse plasma and brains after the systemic administration of this compound. T-401 was orally administered to male C57BL/6J mice (8 weeks old, n = 3) at the dose of 10 mg/kg. Blood and brain samples were collected at 0.5 h after the administration of T-401, and blood was centrifuged to obtain a plasma fraction. Brain samples were weighed and homogenized with four volumes of phosphate-buffered saline. The plasma and brain homogenate samples were deproteinized with acetonitrile. After centrifugation, the supernatant was transferred and concentrated to dryness. The residue was resolved and centrifuged, and the supernatant was injected into LC/MS (see Supplemental Materials for details). Detected metabolites in the brain were also analyzed according to the following HPLC condition: column, Atlantis T3 3 µm 4.6 × 150 mm; mobile phase, acetonitrile/H_2O, (40/60); flow rate, 1.0 mL/min; detection wavelength, 254 nm.

Radiometabolite analysis of [^{18}F]T-401 in the mouse brain

After the i. v. injection of [^{18}F]T-401 into C57BL/6J mice (n = 4), these mice were sacrificed by cervical dislocation at 1, 5, 10, 30, and 60 min. Brain samples were quickly collected and processed, as previously reported.[13] An aliquot of the supernatant (100–300 µL) prepared from the brain homogenate was analyzed according to the following HPLC condition: column, Atlantis T3 3 µm 4.6 × 150 mm; mobile phase, acetonitrile/H_2O, (40/60); flow rate, 1.0 mL/min; and detection wavelength, 254 nm. The percentage

ratio of unchanged [^{18}F]T-401 to the total radioactivity (corrected for decay) on the HPLC chromatogram was calculated as (peak area for [^{18}F]T-401/total peak area) × 100.

In this analysis, the major radiometabolite of [^{18}F]T-401 in the brain was identified as M_3. The following *in vitro* parameters of M_3 were assayed as described previously:[13] concentration inducing 50% inhibition of human MAGL activity (IC_{50}) and LogD (measured at pH = 7.4).

To further characterize M_3, we radiosynthesized [^{18}F]M_3 and performed the PET imaging of WT mice and MAGL-KO mice after the injection of this radiocompound. Detailed procedures are described in the Supplemental Methods section.

Statistics

Goodness of fit of compartment models was evaluated using the Akaike Information Criterion (AIC)[17] and the Model Selection Criterion (MSC),[18] and F-test.[19]

Results

Arterial input function

Arterial plasma assays illustrated that rates of the decrease in [^{18}F]T-401 and the increase in its radiometabolites were similar among monkeys examined here (Figure 1(a)). Parent fractions rapidly declined and accounted for approximately 30% at 30 min after [^{18}F]T-401 injection in PET experiments at baseline and under blockade with JW642, although there was a tendency that the metabolic conversion of [^{18}F]T-401 was accelerated with an increasing dose of JW642 (Figure 1(b)). Radioactivity concentrations in blood and plasma were also slightly different between conditions with and without JW642 (Figure 1(c) and (d)). As a combined consequence of these differences, metabolite-corrected arterial input functions in blockade studies were considerably distinct from the baseline data (Figure 1(c) and (d)).

PET imaging of rhesus monkeys

Representative baseline PET and corresponding MR images of the rhesus monkey brain are shown in Figure 2(a). TACs for [^{18}F]T-401 in the monkey brains at baseline and under blockade with JW642 at the highest dose (0.3 mg/kg) are also displayed in Figure 2(b) and (c), respectively. [^{18}F]T-401 readily entered the brain with its uptake peaking at 5–15 min after the injection, followed by the highest retentions in the striatum and frontal and occipital cortices, moderate retentions in the thalamus, cerebellum, and hippocampus, and the lowest retentions in the brainstem at

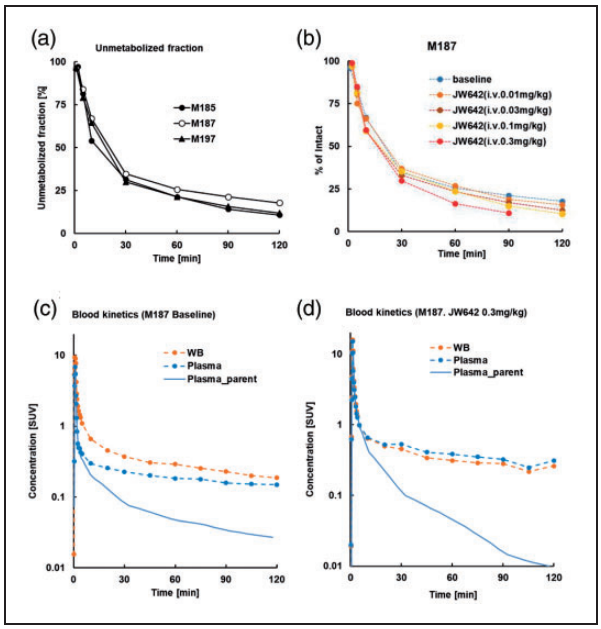

Figure 1. (a, b) Unmetabolized [^{18}F]T-401 fraction in plasma over time in a baseline study of three rhesus monkeys (○M185, ●M187, ▲M197) (b) and in baseline and blockade studies of a rhesus monkey (M187) (b). Metabolic data at 120 min were unavailable in a blockade assay with 0.3 mg/kg of JW642. (c, d) Blood (orange dashed lines), plasma (sky-blue dashed lines) and plasma parent (solid sky-blue lines) radioactivity concentrations at baseline (c) and following pretreatment with 0.3 mg/kg of JW642 are plotted in logarithmic scale (d).

baseline (Figure 2(b)), These data were consistent with known MAGL distributions in the brain.[13] The pretreatment of a monkey with an intravenous injection of 0.3 mg/kg of JW642 resulted in reduced [^{18}F]T-401 retentions with minimum regional differences (Figure 2(c)).

Quantification of [^{18}F]T-401 binding in monkey brains

We evaluated analytical methods to quantify V_T using baseline PET scans of the monkey brains. The ratio of the brain tissue radioactivity to the plasma radioactivity of unmetabolized [^{18}F]T-401 plateaued at approximately 60 min after the radioligand injection at baseline (Supplemental Figure 3 A), indicating reversible binding of [^{18}F]T-401 to MAGL in the monkey brain. Then, TACs for [^{18}F]T-401 at baseline were fitted by the 1-tissue compartment model (1TCM, consisting of compartments C_p and C_1 depicted in Figure 3(a)) and the 2-tissue compartment model (2TCM, consisting of compartments C_p, C_1, and C_2 depicted in Figure 3(a)) assuming reversible radiotracer binding. All these TACs were better described by 2TCM than by 1TCM (Figure 3(b)). Correspondingly, mean AIC and MSC

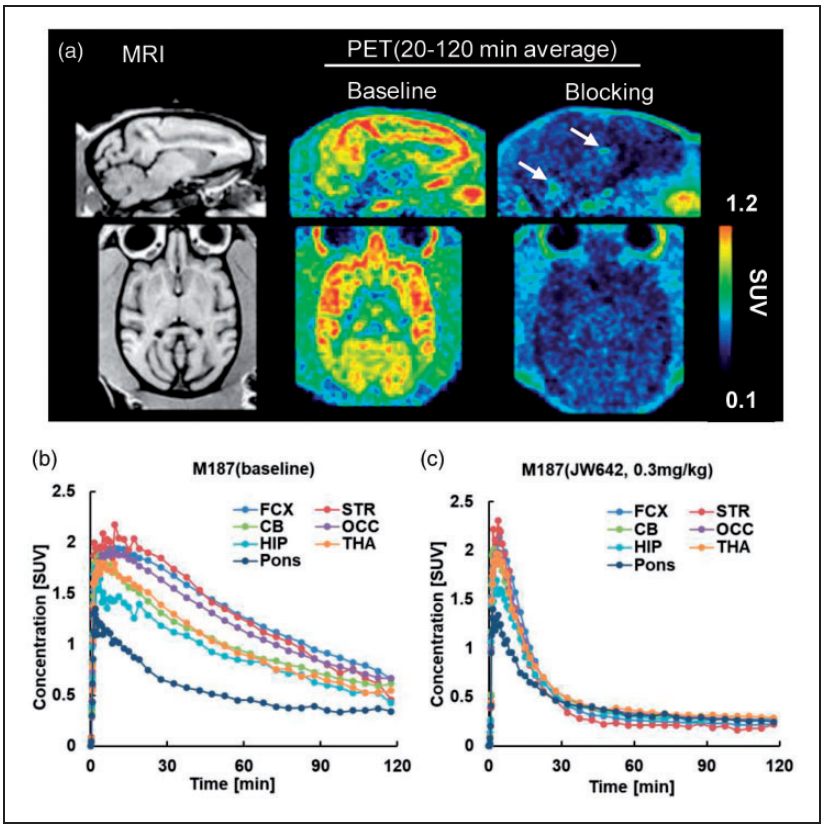

Figure 2. (a) Sagittal (upper) and axial (lower) MR(left) and PET images at baseline (center) and following pretreatment with 0.3 mg/kg of JW642 (right). PET images were generated by averaging dynamic scan data at 60–120 min. Arrows in the sagittal PET image under the blocking condition indicate radioactivity accumulations in the choroid plexus. (b, c) TACs for [^{18}F]T-401 at baseline (b) and following pretreatment with 0.3 mg/kg of JW642 (c). FCX: frontal cortex; STR: striatum; CB: cerebellum; OCC: occipital; HIP: hippocampus; THA: thalamus.

were −18.0 and 4.65, respectively, in the 2TCM fit, and 63.0 and 2.96, respectively, in the 1TCM fit, which indicated that 2TCM was a more suitable model. The F-test also supported the superiority of 2TCM compared to 1TCM for all regions ($p < 0.001$). Accordingly, V_T was calculated as $K_1/k_2\ (1 + k_3/k_4)$, where K_1 [mL/min/cm^3] and k_2 [min^{-1}] represent the influx and efflux of the radioligand across the blood-brain barrier (BBB), respectively. By contrast, 2TCM did not yield a good fit in blockade studies particularly with a high dose of JW642 (Figure 3(b)), and k_4 was estimated as zero in several regions. Unlike the baseline condition, the ratio of brain tissue radioactivity to the plasma radioactivity of unmetabolized [^{18}F]T-401 increased over time in the blockade study (Supplemental Figure 3B). Therefore, it is possible that [^{18}F]T-401 was metabolized in the brain, with its major radiometabolite barely undergoing clearance from the brain following the pretreatment with JW642. We therefore modified 2TCM by incorporating an additional compartment representing a radiometabolite that was irreversibly converted from [^{18}F]T-401 in the brain (2-tissue plus the metabolite compartment model denoted as 2 T + mCM; Figure 3(a)). TACs in a blockade experiment were well described by 2 T + mCM compared to 2TCM, as demonstrated by a fit to cerebellar data shown in Figure 3(b). To evaluate the model suitability, AIC and MSC values were compared between 2 T + mCM and 2TC, and 2 T + mCM yielded smaller AIC and larger MSC values than 2TCM in all ROIs except the striatum (Supplemental Table 1). Similarly, the F values for the comparison of the goodness of fit by 2 T + mCM versus 2TCM were positive in all these areas but the striatum, with the statistically significant superiority of 2 T + mCM over 2TCM in the cerebellum and hippocampus ($p < 0.05$) (Supplemental Table 1). These data support the notion that 2 T + mCM is a more suitable model to describe the kinetics of [^{18}F]T-401 under a blockade condition. The reason why 2 T + mCM did not produce a better fit than 2TCM remain undetermined, but it is presumable that the striatal metabolic conversion of T-401 is relatively slow, in view of the fastest radioactivity washout following the peak uptake

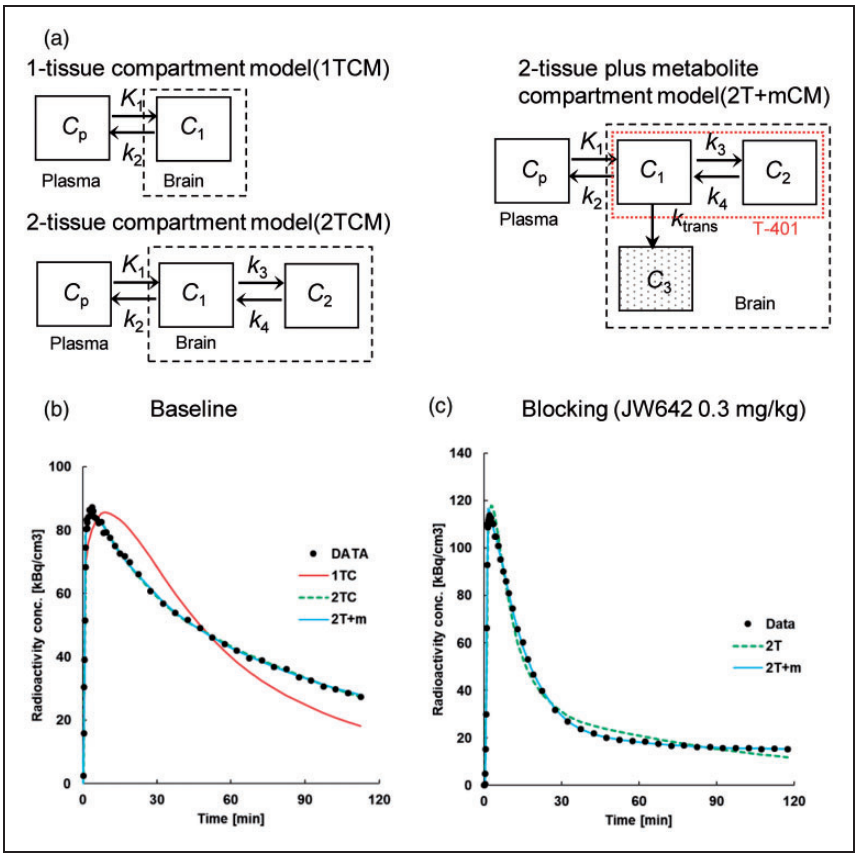

Figure 3. (a) 2 T + mCM constructed as modification of 2TCM by adding a compartment (C_3) for a radiometabolite converted from parent [^{18}F]T-401 in the brain (c). K_1, k_2, k_3, k_4 and k_{trans} denote rate constants for the transfer of a radiocompound between different compartments. Red dotted rectangle represents the range of [^{18}F]T-401 distribution in the brain. (b, c) Compartment model fits to cerebellum TACs at baseline (b) and following pretreatment with 0.3 mg/kg of JW642 (c). At baseline (b), 2TCM (green line) better described cerebellar TAC (black circles) than 1TCM (red line). Under blockade by JW642 (c), 2 T + mCM (solid sky-blue line) offered a better fit to cerebellar TAC (black circles) than 2TCM (green line).

in this area (Figure 2(b) and (c)). According to these results, to follow a consistent analytical protocol, we initially fitted 2 T + mCM to the all TACs. For securing the fitting stability, k_{trans} [min^{-1}], a rate constant for the metabolic conversion of the radioligand, was fixed to zero in case that the initial fitting yielded k_{trans} below 0.0001. Likewise, k_3 [min^{-1}], a rate constant for the association of the radioligand with a specific target, was constrained to zero in case that the initial fitting yielded a negligibly small value of k_4, a rate constant for the dissociation of the radioligand from the target. Then, V_T, total distribution volume of unmetabolized [^{18}F]T-401, was calculated as K_1/k_2 $(1 + k_3/k_4)$. In a condition with constrains of k_3 and k_4 to zero, V_T was determined as K_1/k_2. Concerning V_T calculated by 2 T + mCM, changes in this parameter value by truncating dynamic scan data from 120 min to 80 min were less than 5% at baseline and following pretreatment with JW642 (Figure 4), which demonstrated the validity of the scan duration of 120 min for the robust estimation of V_T.

Mean V_T values in three monkeys were the highest in the frontal cortex (11.7 mL/cm^3), followed by the occipital cortex (9.96 mL/cm^3), striatum (9.05 mL/cm^3), and the lowest in the pons (4.73 mL/cm^3) (Table 1).

Occupancy of MAGL by JW642 in the monkey brain as assessed by [^{18}F]T-401-PET

Next, we assessed the capability of ^{18}F-T-401-PET to quantify the occupancy of MAGL by JW642 administered at different doses. The dose-dependent pretreatment of a monkey with JW642 provoked a reduction in the V_T values for [^{18}F]T-401 in all examined brain regions, including the brainstem (Table 2). This result also indicates that the reference tissue model is not applicable to the measurement of [^{18}F]T-401 binding in the monkey brain.

A global measure of the MAGL occupancy by JW642 was calculated using Lassen's graphical plot analysis of V_T values estimated by 2 T + mCM in

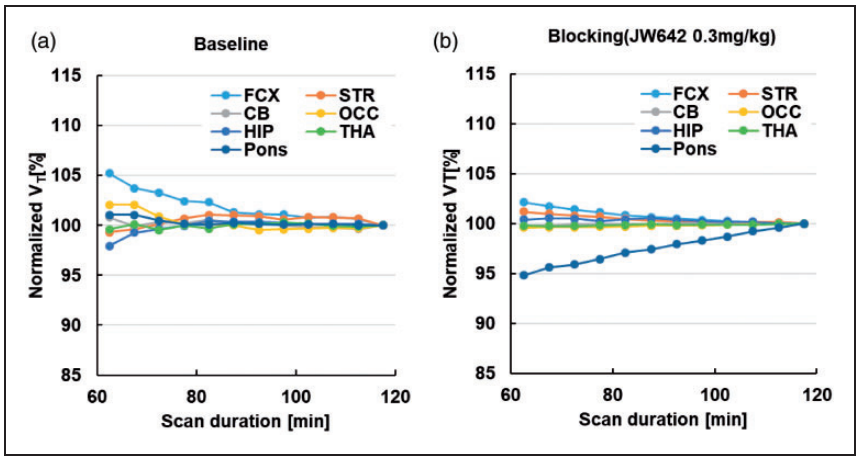

Figure 4. Time-stability of V_T values at baseline (a) and following pretreatment with 0.3 mg/kg of JW642 (b). FCX: frontal cortex; STR: striatum; CB: cerebellum; OCC: occipital; HIP: hippocampus; THA: thalamus.

Table 1. Individual V_T values [mL/cm^3] of three monkeys under the baseline condition.

Region	M197	M187	M185	mean	sd
FCX	11.6	13.5	10.1	11.7	1.7
STR	8.15	12.51	6.48	9.05	3.11
CB	6.85	9.17	5.50	7.17	1.86
OCC	9.17	11.89	8.82	9.96	1.68
HIP	5.41	7.55	4.90	5.95	1.41
THA	4.50	8.58	6.02	6.36	2.06
Pons	4.13	3.48	6.59	4.73	1.64

FCX: frontal cortex; STR: striatum; CB: cerebellum; OCC: occipital cortex; HIP: hippocampus; THA: thalamus.

Table 2. Regional V_T [mL/cm^3] values under baseline and JW642 pretreatment conditions.

		JW642			
Region	Baseline	0.01 mg/kg	0.03 mg/kg	0.1 mg/kg	0.3 mg/kg
FCX	13.5	11.2	7.16	7.20	1.56
STR	12.5	10.6	6.76	6.41	1.40
CB	9.17	6.77	4.95	4.97	1.32
OCC	11.9	8.80	5.41	5.64	1.37
HIP	7.55	6.49	3.71	4.27	1.17
THA	8.58	7.62	4.10	4.59	1.32
Pons	3.48	2.89	1.89	2.31	0.808

different brain regions.[20,21] Occupancy values ranged from 20% by the lowest dose of JW642 (0.01 mg/kg) to 94% by the highest dose (0.3 mg/kg) (Supplemental Figure 4). The non-displaceable distribution volume (V_{ND}) was calculated as an averaged x-intercept of the regression lines and was 0.69 mL/cm^3.

An effective concentration of an inhibitor in plasma that induced the 50% occupancy of MAGL (EC_{50}) was calculated by the implementation of the following

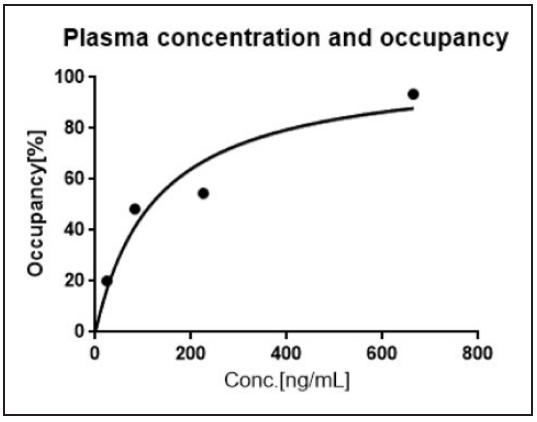

Figure 5. Relationship between plasma JW642 concentration and occupancy of MAGL by JW642. V_{ND} value (0.69 mL/cm^3) and the MAGL occupancy by each dose of JW642 were determined by Lassen's plot analysis (Supplemental Figure 3).[19,20]

equation that is based on Hill's plot of the occupancies versus plasma inhibitor concentration (c): $Occ = c/(c + EC_{50})$ (Graph Pad Prizm 6, GraphPad Software, Inc.); EC_{50} for JW642 was estimated to be 126.1 ng/mL (Figure 5).

Structural identification and characterization of T-401 metabolites in mice

To further obtain supplementary data supporting the use of 2 T + mCM to describe the kinetics of [^{18}F]T-401 in the brain, we analyzed the metabolites of T-401 in mice. Plasma and brain samples collected from mice after T-401 administration were profiled by liquid chromatography – UV detection (LC/UV) and LC/MS. A total of 4 fluoro-containing metabolites (M_1 – M_4) were observed in plasma by LC/UV, and two of these metabolites (M_1, M_3) were detected in the brain

by LC/MS (Supplemental Figure 5). Then, we quantified the radiometabolites of [^{18}F]T-401 in the mouse brains after the intravenous administration of this radiotracer. The fraction of [^{18}F]T-401 in the mouse brain decreased over time, and its polar radiolabeled metabolite, which corresponded to [^{18}F]M_3, according to its retention time, was determined from the HPLC chart (Supplemental Figure 1). The fraction of [^{18}F]M_3 in the mouse brain was increased to approximately 25% of the total radioactivity at 60 min after the injection of [^{18}F]T-401 (Supplemental Figure 6). The *in vitro* characterization of M_3 demonstrated that M_3 exhibited a very low LogD value (0.42) and a weak MAGL inhibitory activity with IC_{50} exceeding 10000 nM. As expected from its *in vitro* profile, [^{18}F]M_3 exhibited a very poor BBB penetration and low brain uptake in the brains of these mice throughout the scanning time (Supplemental Figure 7).

Discussion

In the current study, we demonstrated the quantitative evaluation of MAGL and its occupancy by JW642 in the monkey brains using PET with [^{18}F]T-401. In line with the reversibility of [^{18}F]T-401 binding in the brain, the retention of this radioligand can be quantified with plasma and brain tissue TACs over 120 min. In blockade experiments, Lassen's plots consisting of data from multiple ROIs were linearity presented, which supported the validity of the assumption that V_{ND} for [^{18}F]T-401 is uniform among these brain regions. This feature of [^{18}F]T-401 allowed to measure MAGL occupancy by JW642 at different doses, which allowed to the successfully determine the plasma EC_{50} of JW642 by Hill's plot.

The radiometabolite analysis in monkey plasma showed a considerably rapid metabolic conversion of [^{18}F]T-401, with the radiometabolites accounting for approximately 70% of the total radioactivity at 30 min after intravenous injection. The slight acceleration of the peripheral radioligand metabolism was observed in the presence of JW642, and this change was presumably attributable to an increase in MAGL-unbound [^{18}F]T-401, which was prone to biometabolism, as a consequence of the MAGL inhibition by JW642 in peripheral tissues. In the monkey brain, [^{18}F]T-401 displayed a fast uptake, followed by a moderate washout from all regions, as previously reported.[13] After the pretreatment with JW642 at the highest applied dose (0.3 mg/kg, i. v.), the radioactivity retention considerably decreased to a low and uniform level among brain regions, which indicated that retentions of MAGL-unbound radioligands (and their radiometabolites) were similar across these areas. As the brainstem, which showed the lowest uptake of [^{18}F]T-401, exhibited displaceable radioligand binding, the radioligand kinetics could not be analyzed by a reference tissue model. Therefore, we estimated V_T as a quantitative measure that reflected [^{18}F]T-401 binding in the brain using the arterial plasma input function. 2TCM produced suitable fits to all regional TACs at baseline but did not yield a good fit to TACs in blocking studies. Therefore, the unsuitability of 2TCM under the blockade of MAGL is likely to result from the effects of radiometabolites on the tissue radioactivity, as the tissue-to-plasma ratio of radioactivity continued to increase over 120 min in the blocking experiments (Supplemental Figure 3), which implied the accumulation of radiometabolites in the brain. Thus, it was initially hypothesized that radiometabolites in the brain either transferred from plasma or produced by *in-situ* conversion from [^{18}F]T-401 were increased as a result of elevated levels of MAGL-unbound, metabolism-prone [^{18}F]T-401 following the blockade of MAGL by JW642. However, the early radioactivity uptake into the brain did not overtly increase in the blocking experiments, which does not support the possibility of a blockade-induced increases of unbound radioligands and their metabolites to be transferred to the brain. We also analyzed TACs under the blocking condition with several compartment models by assuming the entry of a plasma radiometabolite into the brain, but these models did not improve the goodness of fit relative to 2TCM (data not shown). In contrast, 2 T + mCM provided suitable fits to the observed data at baseline and after the pretreatment with JW642, which is indicative of conversion of [^{18}F]T-401 to the major radiometabolite in the brain. In fact, it seems that a pseudo-equilibrium of the radioligand kinetics was reached faster under the MAGL blockade than was it at baseline (compare Supplemental Figures 3 A and 3B), followed by a progressive increase of the radioactivity in the brain, presumably resulting from gradual accumulations of the radiometabolite. Despite this indication, it could also be ruled out that the continuous elevation of tissue-to-plasma ratio in the blocking experiments is attributable to faster elimination of plasma unchanged [^{18}F]T-401 by acceleration of peripheral metabolism (Figure 1(b) and (d)), leading to an unreachable equilibrium of the tracer kinetics between the plasma and brain by 120 min.

To support the validity of 2 T + mCM for describing the kinetics of [^{18}F]T-401 in the brain, we identified four fluorinated metabolites ($M_1 - M_4$) in plasma samples from mice after administration of non-radiolabeled T-401. Then, we found that [^{18}F]M_3, which can be generated by the hydrolysis of [^{18}F]T-401, was the most abundant radiometabolite in the mouse brain. The *in vitro* and *in vivo* characterization

of M_3 suggested that M_3 did not react with MAGL and that the transfer of M_3 between plasma and the brain is limited owing to its high polarity. These data support the view that [^{18}F]M_3 can be generated from [^{18}F]T-401 in the monkey brain, which results in its on-site accumulation without binding to MAGL, and this notion is in line with 2 T + mCM.

In the striatum of a monkey, k_4 was estimated to be close to zero at baseline, and such negligibly small k_4 values were more frequently observed with an increasing dose of blocking JW642 (Supplemental Table 2). As our baseline PET data supported the reversibility of the specific radioligand binding, we constrained both k_3 and k_4 to zero in these cases, assuming the paucity of the available binding components. This parameter fixation could help circumvent the instability of the fitting process. However, the occupancy of MAGL by the highest dose of JW642 (0.3 mg/kg) was 93%, and the constraint of k_3 and k_4 to zero might result in the estimation of K_1, k_2, and k_{trans} based on a local minimum in the proximity of the true solution in the goodness-of-fit space.

We also noted that the cerebellum, hippocampus, and pons exhibited higher k_{trans} than other areas. These regions are adjacent to the choroid plexus, where increased radioactivity retention was observed under blocking conditions (Figure 2(a) and Supplemental Figure 9). Therefore, it is conceivable that radioactivity spill-in from the choroid plexus affected the estimation of k_{trans}. Indeed, k_{trans} estimates were decreased when the cerebellar ROI was defined to cover the ventral portion only, which was distant from the choroid plexus (Supplemental Figure 9). Meanwhile, there was a tendency that k_{trans} in all regions increased under the blockade of MAGL relative to the baseline, raising a possibility of direct or indirect interactions between MAGL and T-401-catalyzing enzyme. To examine this notion, we carried out an additional [^{18}F]T-401-PET experiment in two monkeys treated with a new MAGL inhibitor, compound 4f, the chemical structure of which is distinct from the chemical class of JW642. The dosage of this compound (0.85 mg/kg, oral administration) induced a full occupancy of MAGL in the brain, and 2 T + mCM better described the radioligand kinetics than 2CT in this condition. In addition, k_{trans} was increased in most regions relative to the baseline, with the values in the hippocampus and cerebellum higher than other areas (compare Supplemental Tables 2 and 4). In addition, it is presumable that the water-soluble radiometabolites produced in the brain could be transferred to the ventricles and accumulate in the choroid plexus, implying that the effect of the spillover was dependent on the rate of the metabolic conversion reflected by k_{trans}. Although these preliminary data support the utility of 2 T + mCM during the blockade of MAGL, which may alter the metabolic rate of T-401, the biological significance of k_{trans} will need to be further investigated by identification of this enzyme and *ex vivo* measurements of its activities in the baseline and blocking conditions.

Our time-stability assessments also indicated that V_T can be robustly estimated by analyzing the 120-min scan data with 2 T + mCM (Figure 4(b)). Moreover, the rank order of regional V_T values at baseline estimated with 2 T + mCM was consistent among three monkeys and was in good agreement with the local distribution of autoradiographic [^{18}F]T-401 binding in monkey brain slices (Supplemental Figure 8).

The blocking studies demonstrated the occupancy of MAGL by JW642 in a dose-dependent manner and the predominance of specific [^{18}F]T-401 binding versus non-specific radioligand binding at baseline. V_T, which is a parameter of the total radioligand binding, is the sum of the distribution volumes of specific (V_S) and non-specific (V_{ND}) bindings. The V_{ND} value, which was estimated with Lassen's plot, was 0.69 mL/cm^3, whereas the mean V_T values ranged from 4.73 (pons) to 11.7 (striatum) mL/cm^3. Therefore, V_{ND} accounted for a relatively small portion of V_T, ranging from 0.06% (striatum) to 14.6% (pons). The high contrast for specific versus non-specific binding components would be a notable benefit of PET scans with [^{18}F]T-401, and the wide range of V_T among brain regions facilitates the precise calculation of MAGL occupancies by an exogenous inhibitor using Lassen's plot. Since the diversity of regional V_T values may stem from the regionally variable concentration of the radioligand binding sites (B_{max}), we performed an auxiliary *in-vivo* Scatchard plot analysis of the baseline [^{18}F]T-401-PET data to determine the dissociation constant (K_D) of the ligand and B_{max} values in several representative ROIs (Supplemental Figure 10 and Supplemental Table 3; methods are provided in Supplemental Materials and Methods). K_D ranged from 1.09 nM (hippocampus) to 4.18 nM (frontal cortex), and B_{max} values in the frontal and occipital cortices, cerebellum, and hippocampus were ranked in this order, ranging from 32.9 (hippocampus) to 119.7 (frontal cortex). These results were in fairly good agreement with the data in the literature.[13,22] Meanwhile, the accuracy of the measurements was not secured due to relatively narrow ranges of the bound ligand concentration and bound-to-free ligand ratio and fixation of the free ligand fraction in the brain to 1.

[^{18}F]T-401 has been recently applied to a PET study in humans, and the quantification of MAGL in the human brain with this radioligand is underway. Once [^{18}F]T-401 is fully validated in human subjects, it can provide critical information on the target engagement of a candidate drug acting on MAGL. The quantitative

assays of MAGL levels in the human brain by [^{18}F]T-401-PET would also help to clarify the roles played by this enzyme in neuropsychiatric conditions, which would further confirm the use of MAGL inhibitors as potential therapeutics.

Conclusion

In this study, we demonstrated that the pharmacokinetics of [^{18}F]T-401 in the monkey brains was robustly described by a reversible binding model, which was also valid in quantifying the blockade of radiotracer binding by a MAGL inhibitor JW642. These observations support the utility of [^{18}F]T-401 for the PET assays of MAGL in healthy and diseased conditions and for the *in vivo* evaluations of interactions between MAGL and candidate therapeutics. Based on its favorable properties as an imaging agent, this novel MAGL PET ligand was advanced to further evaluation in humans. The results from the human study will be reported in the future.

Funding

The author(s) disclosed receipt of the following financial support for the research, authorship, and/or publication of this article: This study was funded by Takeda Pharmaceutical Company Limited (TAKEDA).

Acknowledgments

The authors thank Mr. Mikio Shirasaki for metabolite structure analysis and the staff at the former National Institute of Radiological Sciences for their assistance with the cyclotron operation, radioisotope production, radiosynthesis, and animal experiments.

Declaration of conflicting interests

Y.H., K.A. and T.K. are current or former employees of TAKEDA. C.S., J.M., Y.N., Z.MR., T.M. and M.H. are current or former employees of National Institutes for Quantum Science and Technology. No other potential conflicts of interest relevant to this article exists.

Authors' contributions

All authors contributed to the study conception and design. Material preparation, data collection and analysis were performed by Yasushi Hattori, Chie Seki, Jun Maeda, Yuji Nagai and Kazunobu Aoyama. The first draft of the manuscript was written by Yasushi Hattori and Chie Seki, and Makoto Higuchi, Tatsuki Koike, Ming-Rong Zhang and Takafumi Minamimoto commented on previous versions of the manuscript. All authors read and approved the final manuscript.

Supplemental material

Supplemental material for this article is available online.

ORCID iD

Takafumi Minamimoto https://orcid.org/0000-0003-4305-0174

References

1. Ahn K, McKinney MK and Cravatt BF. Enzymatic pathways that regulate endocannabinoid signaling in the nervous system. *Chem Rev* 2008; 108: 1687–1707.
2. Di Marzo V, Melck D, Bisogno T, et al. Endocannabinoids: endogenous cannabinoid receptor ligands with neuromodulatory action. *Trends Neurosci* 1998; 21: 521–528.
3. Pacher P, Bátkai S and Kunos G. The endocannabinoid system as an emerging target of pharmacotherapy. *Pharmacol Rev* 2006; 58: 389–462.
4. Bisogno T and Di Marzo V. Short- and long-term plasticity of the endocannabinoid system in neuropsychiatric and neurological disorders. *Pharmacol Res* 2007; 56: 428–442.
5. Savinainen JR, Saario SM and Laitinen JT. The serine hydrolases MAGL, ABHD6 and ABHD12 as guardians of 2-arachidonoylglycerol signaling through cannabinoid receptors. *Acta Physiol (Oxf)* 2012; 204: 267–276.
6. Blankman JL, Simon GM and Cravatt BF. A comprehensive profile of brain enzymes that hydrolyze the endocannabinoid 2-arachidonoylglycerol. *Chem Biol* 2007; 14: 1347–1356.
7. Makara JK, Mor M, Fegley D, et al. Selective inhibition of 2-AG hydrolysis enhances endocannabinoid signaling in hippocampus. *Nat Neurosci* 2005; 8: 1139–1141.
8. Nomura DK, Morrison BE, Blankman JL, et al. Endocannabinoid hydrolysis generates brain prostaglandins that promote neuroinflammation. *Science* 2011; 334: 809–813.
9. Piro JR, Benjamin DI, Duerr JM, et al. A dysregulated endocannabinoid-eicosanoid network supports pathogenesis in a mouse model of Alzheimer's disease. *Cell Rep* 2012; 1: 617–623.
10. Fowler CJ. Monoacylglycerol lipase - a target for drug development? *Br J Pharmacol* 2012; 166: 1568–1585.
11. Mulvihill MM, and and Nomura DK. Therapeutic potential of monoacylglycerol lipase inhibitors. *Life Sci* 2013; 92: 492–497.
12. Ming J, and and Mario VS. Activity-Based protein profiling delivers selective drug candidate ABX-1431, a monoacylglycerol lipase inhibitor, to control lipid metabolism in neurological disorders. *J. Med. Chem* 2018; 61: 9059–9061.
13. Hattori Y, Aoyama K, Maeda J, et al. Design, synthesis, and evaluation of (4*R*)-1-{3-[2-[^{18}F]fluoro-4-methylpyridin-3-yl]phenyl}-4-[4-(1,3-thiazol-2-ylcarbonyl)piperazin-1-yl]pyrrolidin-2-one ([^{18}F]T-401) as a novel positron-emission tomography imaging agent for monoacylglycerol lipase. *J Med Chem* 2019; 62: 2362–2375.
14. Chang JW, Niphakis MJ, Lum KM, et al. Highly selective inhibitors of monoacylglycerol lipase bearing a reactive group that is bioisosteric with endocannabinoid substrates. *Chem. Biol* 2012; 19: 579–588.

15. Ikeda S, Sugiyama H, Tokuhara H, et al. Design and synthesis of novel spiro derivatives as potent and reversible monoacylglycerol lipase (MAGL) inhibitors: bioisosteric transformation from 3-Oxo-3,4-dihydro-2H-benzo [b][1,4]oxazin-6-yl moiety. *J Med Chem* 2021; 64: 11014–11044.
16. Fujinaga M, Luo N, Kumata K, et al. Development of ^{18}F-Labeled radiotracer with improved brain kinetics for positron emission tomography imaging of translocator protein (18 kDa) in ischemic brain and glioma. *J Med Chem* 2017; 60: 4047–4061.
17. Akaike. H. A new look at the statistical model identification. *IEEE Trans Automat Contr* 1974; 19: 716–723.
18. Fujita M, Seibyl JP, Verhoeff NP, et al. Kinetic and equilibrium analyses of [(123)I]epidepride binding to striatal and extrastriatal dopamine D2 receptors. *Synapse* 1999; 34: 290–304.
19. Hawkins RA, Phelps ME and Huang SC. Effects of temporal sampling glucose metabolic rates, and disruptions of the blood–brain barrier on the FDG model with and without a vascular compartment: studies in human brain tumors with PET. *J Cereb Blood Flow Metab* 1986; 6: 170–183.
20. Lassen NA, Bartenstein PA, Lammertsma AA, AA, et al. Benzodiazepine receptor quantification in vivo in humans using [11C]flumazenil and PET: application of the steady-state principle. *J Cereb Blood Flow Metab* 1995; 15: 152–165.
21. Cunningham VJ, Rabiner EA, Slifstein M, et al. Measuring drug occupancy in the absence of a reference region: the lassen plot re-visited. *J Cereb Blood Flow Metab* 2010; 30: 46–50.
22. Zhang L, Butler CR, Maresca KP, et al. Identification and development of an irreversible monoacylglycerol lipase (MAGL) positron emission tomography (PET) radioligand with high specificity. *J Med Chem* 2019; 62: 8532–8543.